Computers & Fluids 39 (2010) 1529–1541

Contents lists available at ScienceDirect

Computers & Fluids

journal homepage: www.elsevier.com/locate/compfluid

Numerical investigations on dynamic stall of low Reynolds number flow around oscillating airfoils ☆

Shengyi Wang [a,b,*,1], Derek B. Ingham [b], Lin Ma [b], Mohamed Pourkashanian [b], Zhi Tao [a]

[a] School of Jet Propulsion, Beijing University of Aeronautics and Astronautics, Beijing 100191, China
[b] Centre for CFD, University of Leeds, Leeds LS2 9JT, United Kingdom

ARTICLE INFO

Article history:
Received 24 August 2009
Received in revised form 18 January 2010
Accepted 11 May 2010
Available online 15 May 2010

Keywords:
Dynamic stall
Low Reynolds number
Oscillating blade
Aerodynamics
SST $k-\omega$ turbulence model
VAWT

ABSTRACT

This paper presents a 2D computational investigation on the dynamic stall phenomenon associated with unsteady flow around the NACA0012 airfoil at low Reynolds number ($Re_c \approx 10^5$). Two sets of oscillating patterns with different frequencies, mean oscillating angles and amplitudes are numerically simulated using Computational Fluid Dynamics (CFD), and the results obtained are validated against the corresponding published experimental data. It is concluded that the CFD prediction captures well the vortex-shedding predominated flow structure which is experimentally obtained and the results quantitatively agree well with the experimental data, except when the blade is at a very high angle of attack.

1. Introduction

With the depletion of fossil fuel energy, and the increasing acknowledgement of the importance of developing environmentally friendly energy resources, the wind turbine, as the main technology to extract energy from wind, has been increasingly investigated. From the perspective of urban applications, Vertical Axis Wind Turbines (VAWTs) have many advantages over the widely used conventional Horizontal Axis Wind Turbines (HAWTs) [1–4]. However, VAWTs suffer from many complicated aerodynamical problems, of which dynamic stall is an inherent phenomenon when they are operating at low values of tip speed ratio, $\lambda < 5$[5], and this has a significant impact on vibration, noise, and power output of the VAWTs [6]. Therefore, it is crucial to have a good understanding of the mechanism of dynamic stall, in particular at relatively low Reynolds number ($Re_c \approx 10^5$) appropriate to the urban applications of VAWTs which are not fully understood.

Fig. 1a is a schematic of a straight-bladed fixed-pitch VAWT which is the simplest, but typical form, of the Darrieus type VAWTs. Despite the simplicity, its aerodynamic analysis is still quite complex. One feature is that the relative velocities perceived by the blade always change as the blade moves to different azimuthal positions. Fig. 1b illustrates typical flow velocities around a rotating VAWT blade at a given azimuthal angle θ, as well as the aerodynamic forces perceived by the blade. The azimuthal angle θ is set to be zero when the blade is at the top of the flight path and it increases in a counter-clockwise direction. It should be noted that, even disregarding the variation of the induced local flow velocity U_{local}, both the magnitude and the direction of the effective velocity perceived by the blade, U_{eff}, change in a cyclic manner as the blade rotates through different azimuthal angles. This kind of motion is called the Darrieus motion [7]. As a result, the aerodynamic loads exerted on the blade change cyclically with θ.

From the inset at the bottom right hand corner of Fig. 1b, we can obtain the following expression that establishes the relationship between the anlge of attack α, the tip speed ratio λ and the azimuthal angle θ of a blade performing Darrieus motion (without velocity induction):

$$\tan\alpha = \frac{U_\infty \sin\theta}{\Omega R - U_\infty \cos\theta} = \frac{\sin\theta}{\lambda - \cos\theta} \quad \text{or} \quad \alpha = \arctan\left(\frac{\sin\theta}{\lambda - \cos\theta}\right).$$

A normalised angle of attack α is evaluated from this expression as a fuction of the azimuthal angle θ for various values of λ, as shown in Fig. 2. Since dynamic stall of VAWTs mainly occurs under the circumstances of low values of tip speed ratio ($\lambda \leqslant 5$), the variations

☆ This paper is a collaborative effort.

* Corresponding author at: Centre for CFD, University of Leeds, Leeds LS2 9JT, United Kingdom. Tel.: +44 (0)113 343 2569; fax: +44 (0)113 246 7310.
E-mail addresses: presw@leeds.ac.uk, gmwsy@163.com (S. Wang), D.B.Ingham@leeds.ac.uk (D.B. Ingham), L.Ma@leeds.ac.uk (L. Ma), M.Pourkashanian@leeds.ac.uk (M. Pourkashanian), tao_zhi@buaa.edu.cn (Z. Tao).

[1] Mr. Shengyi Wang is currently a visiting PhD student in the Centre for CFD at The University of Leeds, United Kingdom.

0045-7930/$ - see front matter © 2010 Elsevier Ltd. All rights reserved.
doi:10.1016/j.compfluid.2010.05.004

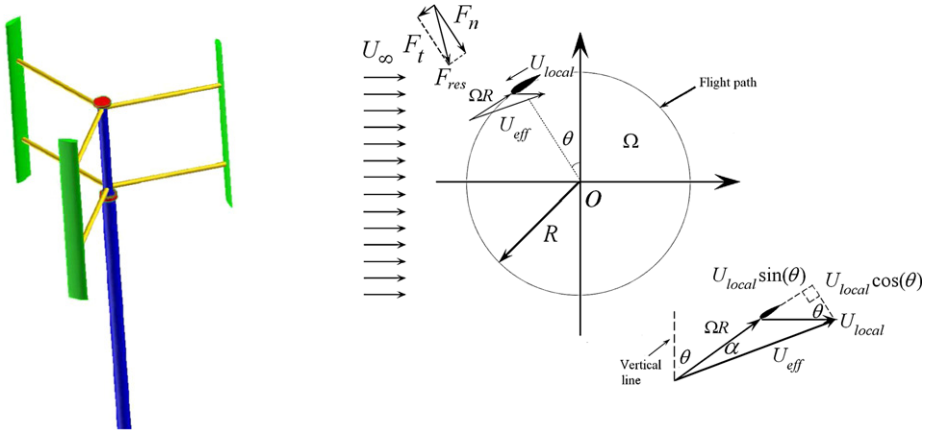

(a) Sketch of a fixed-pitch straight-bladed VAWT.

(b) Typical flow velocities of a straight-bladed Darrieus type VAWT.

Fig. 1. Basics of VAWT.

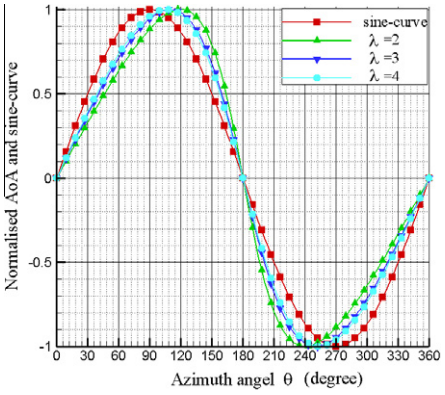

Fig. 2. Comparison between the normalised angle of attack α and the sine-curve ($\alpha = \sin\theta$).

of angles of attack at the low values of λ ($\lambda = 2$, 3 and 3.5) are presented in this figure and compared with the sine-curve, i.e. $\alpha = \sin\theta$. It should be noted that the track of the general variation of the normalised angle of attack, α, of the blade in Darrieus motion, is very similar to the sine-curve. Therefore, in a rotational frame of reference fixed on the turbine blade, the blade would perceive a cyclic variation in the effective air velocity and the angle of attack which is very similar to what would be experienced with a sinusoidally pitching blade in a stationary frame of reference. On the basis of this similarity, it is likely that there may be a similarity with regard to the dynamic stall mechanics for these two types of motion. Therefore, the investigation into the dynamic stall in the relatively simple oscillating airfoils will provide us with significant insight as to what would occur in a real but more complicated VAWT blade. However, it should be noted that there is an element of plunging motion of the blade in the operation of the VAWT and this does not exist in an oscillating aerofoil. Therefore, in the present paper we only focous on the effective pitching motion.

Dynamic stall is a term used to describe the delay in the stall on wings and airfoils that are rapidly pitched with the angle of attack, α, significantly beyond the static stall angle and normally can generate a substantially larger lift for a short period of time than can be obtained quasi-statically [8]. This phenomenon has been involved in a wide range of turbo-machinery, such as jet engine compressor blades, highly manoeuvrable fighters, wind turbines, helicopter rotor blades and even insect wings [6]. Kramer [9] first recognised the dynamic features associated with the dynamic stall in a rapid variation of the incidence experienced by an airfoil. However, the importance of the phenomenon was first identified and emphasized in the helicopter community when helicopter design engineers were confused by the extra lift gained on the helicopter rotor in the retreating phase in the 1960s [6,8].

The stall process can be divided into four key stages, i.e. attached flow, development of the LEV, post-stall vortex shedding, and the reattachment of the flow [9]. Numerous experiments have shown that the flow field for deep dynamic stall is characterised by the initialization, growth, covection and shedding of an intense vortex (LEV) over the suction surface. It is generally accepted that the LEV, carrying a low pressure wave generates a significantly larger lift when the angle of attack is far beyond the angle of static stall until it is shed into the wake. Further the shedding of the LEV causes a sudden breakdown in the lift and a rapid increase in the drag and nose-down pitching moment. It should be emphasized that during the downstroke phase of the pitching cycle, a secondary vortex is often oberseved [10,11], which augments the lift coefficient significantly but this has received little attention. The appearance of the secondary vortex is usually indicated in the lift coefficient curve by a second peak after the peak generated by the LEV. A more detailed description of the dynamic stall events can be found in the review by Carr [6].

Extensive experiments have been performed to study the dynamic stall phenomenon [9–16] and the shedding of LEV has been experimentally represented by many researchers [6]. It has been found that the flow behaviour strongly depends on a number of parameters, such as the shape of the airfoil, mean angle, α_0, amplitude of oscillation, α_l, reduced frequencies, k, and in particular the Reynolds numbers, Re_c, and Mach numbers, Ma [10,13]. In addition to the extensive experimental investigations, a variety of numerical methods have also been applied to analyse the dynamic stall phenomenon [9,17–25] and many reviews based on these results have been published [6,26,27]. However, most of the previous investigations concerned with relatively high higher Reynolds numbers, say, about 1×10^6 or larger. Only a few experimental studies have been published in the low Re regime that is applicable to the VAWTs that are intended for use in the urban environment, where the blades are operating at a relatively low Re_c, typically of the order of 10^5. This paper concentrates on the dynamic stall at this low Reynold number regime ($Re_c \approx 10^5$).

The accuracy of the computational simulations employing URANS is essentially related to the competence of the employed

turbulence model. Many popularly used turbulence models for aerodynamic simulations, such as Baldwin–Lomax, *RNG* $k-\varepsilon$, Spalart-Allmaras, as well as baseline $k-\omega$ model, nonlinear eddy-viscosity models, etc., have been evaluated for the ability of simulating this type of complex flow [21,23,24,28]. However, almost all of the models fail to generate results which can consistently agree well with the experimental data, in particular for those pitching patterns associated with higer angles of attack and high reduced frequency. The *standard* $k-\omega$ model and the *SST* $k-\omega$ model (which is a combination of the *standard* $k-\omega$ and $k-\varepsilon$ models) have been reported to perform well in flows with large separation regions and severe adverse pressure gradients. The description of these turbulence models are detailed in [29,30]. To the best of our knowledge, there is still only a few numerical investigations that employ these models to simulate the dynamic stall phenomenon associated with low Reynolds number (around 10^5) turbulence flow regime. The only papers that we have located that involve low Reynolds number flow are the investigation of Spentzos et al. [24] and the recently published paper by Martinat et al. [31]. Therefore, the objective of this paper is to assess the ability of the *standard* $k-\omega$ model and the *SST* $k-\omega$ model to correctly simulate dynamic stall in the low Reynolds number regime which is found in VAWTs and make a contribution towards a better understanding of the flow physics of dynamic stall in order to assist in the design optimizations of VAWTs intended for the built and urban environment in the future.

2. CFD simulations

2.1. The cases investigated

In this paper, we numerically investigate two experimental cases associated with deep dynamic stall with different blade pitching patterns. Case I is the experimental investigation of Wernert et al. [9] and Case II is from the study of Lee and Gerontakos [16]. In both cases, the blade executes an oscillatory motion around a fixed pivot with the angle of attack following the sinusoidal mode given by the function $\alpha = \alpha_0 + \alpha_l \sin(\omega t)$, but with different mean angles of attack α_0, pitching magnitude α_l and reduced frequency k, see Fig. 3. Table 1 gives a summary of the operating conditions employed in the two experiments.

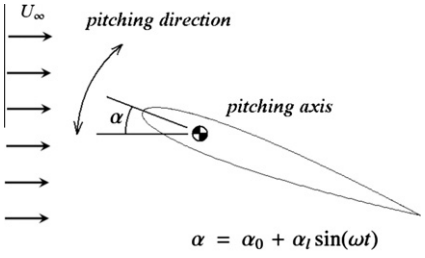

Fig. 3. Illustration of blade pitching motion.

With regard to the reasons for the choice of the two cases, first of all, the range of the Reynolds number is the basic requirement for the purpose of the present research which excludes a large portion of the experimental work. In particular, the Case I is selected primarily due to the availability of the near-wall profiles of velocity magnitude at the airfoil suction side as these are very useful in the validation of the numerical results. In the literature, many investigations into the aerodynamics of the pitching blade motion have reported information on the integral aerodynamic loads and moments on the airfoils but very few present the velocity fields around the airfoil. Unfortunately, experimental data on the instantaneous aerodynamic load loops during a complete pitching cycle that are also essential in order to assess the computational work is not available in this investigation. Therefore, to complement Cases I and II which contains such experimental data is chosen. In addition, the coverage of both positive and negative angles of attack in Case II is what occurs in the real Darrieus type motion.

2.1.1. Case I: Wernert et al. [9]

The airfoil in this case executes the sinusoidal pitching motion $\alpha = 15^\circ + 10^\circ \sin(41.89t)$ with a reduced frequency of $k = 0.15$. The free stream velocity is 28 m/s, resulting in a Reynolds number Re_c of 3.73×10^5, based on the chord length. The experimental investigation was conducted in a low-speed wind tunnel which has an open, rectangular test section of 70 cm in width, 80 cm in length and 90 cm in height. The blade was mounted between two circular end plates with a diameter of 40 cm to ensure a two-dimensional flow in the vertical centre plane of the test section. The dynamic stall process on a pitching NACA0012 airfoil with a chord length of 0.2 m was experimentally investigated employing particle image velocimetry (PIV) and Laser-Sheet Visulisations (LSV).

2.1.2. Case II: Lee and Gerontakos [16]

In this case, the blade oscillates with the sinusoidal mode: $\alpha = 10^\circ + 15^\circ \sin(18.67t)$ with a reduced frequency $k = 0.10$. The free stream velocity is $U_\infty = 14$ m/s, the turbulence intensity is about 0.08%, and the Reynolds number is $Re_c = 1.35 \times 10^5$. The experiment was conducted in a low-speed, suction-type wind tunnel with a wall-bounded test section of 120 cm in width, 270 cm in length and 90 cm in height. The blade was fitted with two end plates with 30 cm in diameter to diminish the end effects. The gaps between the oscillatory airfoil and the stationary end plates were kept within 1*mm* to minimize the leakage of the blade-tip flow.

The transient behaviour of the blade surface unsteady boundary layer and the characteristics of the dynamic stall events associated with an oscillating NACA0012 airfoil were studied using multiple hot-film sensor arrays. In addition, surface pressure measurements

Table 1
Validation case specifications for dynamic stall.

Conditions	Oscillating pattern	Measurement technique
Case I: Wernet et al. [9]		
$Re_c = 3.73 \times 10^5$, $Ma = 0.1$	$\alpha = 15^\circ + 10^\circ \sin(\omega t)$	PIV and LSV,
$U_\infty = 28$ m/s	$\omega = 41.89$ rad/s, $k = 0.15$	low-speed wind tunnel with
NACA0012 with $c = 0.20$ m	pitching axis location from	an open, rectangular test
span = 0.56 m	the leading edge = 0.25*c*	section of 70 cm × 80 cm × 90 cm
Case II: Lee and Gerontakos [16]		
$Re_c = 1.35 \times 10^5$, $Ma = 0.04$	$\alpha = 10^\circ + 15^\circ \sin(\omega t)$	Hot film, hot wire, SV, surface pressure
$U_\infty = 14$ m/s	$\omega = 18.67$ rad/s, $k = 0.10$	measurement, low-speed wind tunnel
NACA0012 with $c = 0.15$ m	pitching axis location from	with a wall-bounded test section of
span = 0.375 m	the leading edge = 0.25*c*	120 cm × 270 cm × 90 cm

and smoke flow visulisations were performed as a supplement to the hot-film data. The aerodynamic forces and moments can be derived from the blade surface pressure measurements.

2.2. Numerical technique

It is well known that there are three main forms of turbulence simulation methods, i.e. Direct Numerical Simulation (DNS), Large Eddy Simulation (LES) and Reynolds-Averaged Navier–Stokes (RANS). DNS, despite being the most advanced computational approach, in which all the space and time scales are resolved, demands huge computing resources and is still too prohibitive to be used in the unsteady complicated simulation involved in the range of Reynolds numbers studied in this paper. Although the computational power has been at a very high level, it is still very computationally expensive to employ LES to numerically investigate the complex unsteady dynamic stall phenomenon since 3D simulations should be performed due to the 3D nature of the eddies. For the present, URANS appears to be the most suitable approach to conduct the dynamic stall flow simulations with an acceptable computational cost and, at least, reasonable accuracy. Therefore, in the present study, the URANS method is employed.

Although the dynamic stall flow studied here is inherently a 3D phenomenon, measurements have been taken to ensure a 2D flow in the mid-span plane, where the experimental data were obtained, in both the two cases investigated. In Case I, the 2D flow in the plane was verified by flow visulisation experiments while in Case II, the 2D uniformity of the flow over the airfoil was found to be within 4% of the free stream value, as checked by a hot-wire probe. Thus, in the present simulations, 2D geometrical configurations are employed to model the experimental investigations and a 2D incompressible unsteady CFD solver, based on the finite volume method in the commercial software package Fluent, is employed to solve the full URANS governing equations. Due to the incompressibility of the flow studied, the pressure-based solver, which employs an algorithm which belongs to the so-called "projection method" and is traditionally implemented to solve low-speed incompressible flows, is chosen. All the governing equations for the solution variables, which are decoupled from each other, are solved sequentially and the SIMPLE algorithm is applied as the pressure-velocity coupling algorithm. With respect to the discretization of the convection terms in the transport equations for the velocity and the turbulence quantities, second-order upwind schemes are utilised. In order to accelerate the rate of convergence of the solution, the algebraic multigrid scheme (AMG) with a V-cycle type for the pressure and a flexible type for the momentum equations is applied. A detailed description of these methods can be found in [32]. The calculations have been carried out using the *standard* $k-\omega$ model, assuming that the flow of the airfoil is fully turbulent and the *SST* $k-\omega$ model with prediction of the laminar-to-turbulence transitional process. The modelling of transition is realised by damping the turbulent viscosity μ_t which is computed as follows with the coefficient α^* [33]:

$$\mu_t = \frac{\rho k}{\omega}\frac{1}{max\left[\frac{1}{\alpha^*},\frac{SF_2}{a_1\omega}\right]}, \quad \text{where} \quad \alpha^* = \frac{0.024 + Re_t/6}{1 + Re_t/6}, \quad Re_t = \frac{\rho k}{\mu\omega}.$$

All the numerical simulations are performed at the same conditions as those of the experimental settings to simulate the flow field at the mid cross-section of the experimental setup.

In order to simulate the sinusoidal pitching motion of the blade, the dynamic-mesh technique is employed. As illustrated in Fig. 4a, the mesh is composed of two sub-domains, one fixed mesh zone and one dynamic mesh zone, both of which are meshed by quadrilateral elements. For the purpose of obtaining a better control of the mesh distribution and a higher resolution of the flow near the blade, the dynamic zone, which is considered to be the region of most interests and require the finest grids, is divided into two parts, namely *sub-grid I* and *sub-grid II*, of which *sub-grid I* is meshed by a structured *C*-grid, as shown in Fig. 4b. Corresponding to the pitching motion of the blade in reality, the circular-shaped dynamic zone containing the blade geometry, i.e. both the *sub-grid I* and *sub-grid II*, pitches like a rigid body with the same sinusoidal mode, $\alpha = \alpha_0 + \alpha_l \sin(\omega t)$, as the blade, whilst the fixed mesh zone is kept stationary. The two zones communicate via a pair of circular interfaces between them. To this end, a UDF subroutine is developed and attached to the Fluent solver to control the dynamic mesh motion. The most refined grid is *sub-grid I* which defines the geometry of the airfoil and its immediate wake development flow region. The grid for Case I has 366 nodes on the suction side of the blade and 200 nodes on the pressure side. The height of the first row of cells is set at a distance to the wall of $10^{-5}c$ and this corresponds to $y^+ \leqslant 0.8$. For the purpose of accurately resolving the boundary layer behaviour, and thus the aerodynamic loads on the airfoil, no wall function is employed and hence the values of y^+ should be less than 1.0 [32]. The total number of meshes is of the order of 10^5. The non-slip boundary condition is used in this simulation to model the opening test section. The independence of the solution on the grid has been achieved by comparing the solutions obtained with the current mesh and a refined mesh, in which the regions of interest, such as the zones near the blade and its wake, have been refined.

A similar meshing strategy to Case I is used for Case II, with the exception that the slip boundaries used in the former mesh are replaced by non-slip boundaries in order to represent the wall of the wind tunnel.

Since the work of Wernert et al. [9], Case I, was performed in an open test region, the computational domain consists of two slip boundaries which are 16*c* and 12*c* away from the blade, respectively, see Fig. 4a. The two slip boundaries have been placed sufficiently far away to eliminate their effect on the flow near the blade. The inlet and outlet boundaries are placed respectively 8*c* upstream and 45*c* downstream of the blade, making the uniform freestream velocity boundary condition at the inlet accurate enough and allowing a full development of the wake. The effects of the size of the computational domain on the numerical solution have been evaluated by extending the boundary of the solution domain step-by-step and finally the aforementioned domain size is considered to be sufficiently large to represent the opening test conditions. The reason why the upper boundary is set to be further than that of the lower is mainly due to the range of values of α, which is always positive in this case, from 5° to 25°, and the complexity of the flow structure on the suction side, or upper side of the blade, such as large separations in the region above the blade. It is pointed out that the determination of the dimensions of the external boundaries is carried out employing a steady case when the blade remains at the largest AoA ($\alpha = 25°$) in consideration of the high cost of the unsteady simulations. Nevertheless, according to other computational simulations conducted by other researchers [9,24], in which the external boundaries were commonly set to be about 10*c* from the blade, the dimensions used here is sufficiently large. It should be noted that the freestream turbulence intensity is less than 0.25% according to the experiment but this was not accurately measured and probably this is because it was technically difficult to accurately obtain the turbulence quantities when the equipment was being employed in 1996. Nevertheless, in the numerical calculations presented in this paper we choose this value to be 0.25%. The effects of the turbulence level on the numerical predictions are discussed later in the next section.

Different time step sizes have been tested and finally a non-dimensional time step of Δt_{nd} about 7×10^{-3} is found to be

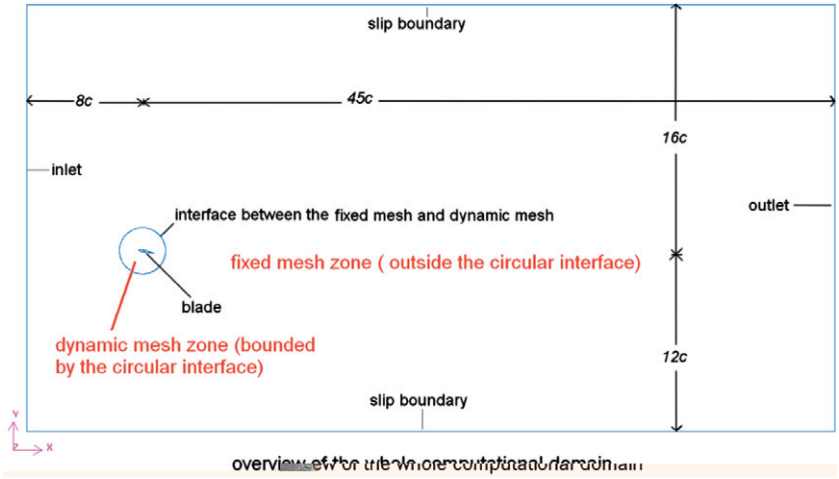

(a) Diagram of the model geometry, boundary conditions and mesh structure.

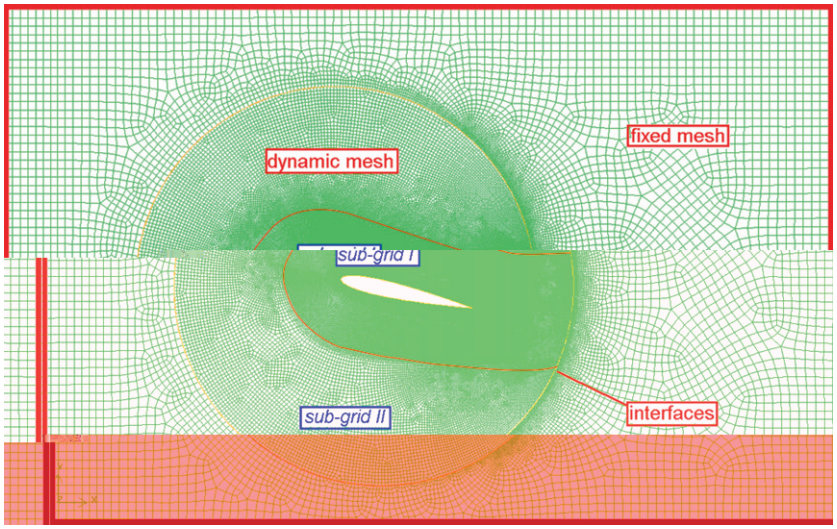

(b) Diagram of the sub-grid structure.

Fig. 4. Computational setup.

Table 2
Residual convergence criterion for all the solution quantities.

Variable	Continuity equation	u_x	u_y	k	ω
Convergence criterion	$\leqslant 10^{-5}$	$\leqslant 10^{-7}$	$\leqslant 10^{-7}$	$\leqslant 10^{-9}$	$\leqslant 10^{-8}$

sufficiently small for the time-independent solution to be obtained for the two cases studied and this has been achieved by checking the time history of C_l, C_d and C_m. The calculations start from an initial flow field obtained from a well converged steady state computation where the airfoil is positioned at the mean angle of attack and, in order to remove the influence of the initial flow field, a sufficient number of cycles of the airfoil pitching motion have been calculated until a periodic solution is achieved for Case I. However, for Case II, due to the severe fluctuations of the computed forces, only a quasi-periodic solution is obtained. Regarding the convergence criteria, the residual for the continuity equation is set to be less than 10^{-5}. See Table 2 for the details of all the computed quantities. In order to confirm that the criteria is sufficient to ensure the convergence of solutions within one time step, the residual for the continuity equation is reset to 10^{-4}. We found that almost no differences can be found between the two set of solutions and this indicates that the current convergence criteria is sufficient to produce converged solutions within one time step in the present study.

3. Results and discussions

3.1. Simulations of the Wernert et al. [9] test case, Case I

For this case, two variants of the $k-\omega$ model, namely the *standard* $k-\omega$ model ($sk\omega$) and the *SST* $k-\omega$ model ($SSTk\omega$) are assessed. As mentioned in the introduction, the primary merit of this case is the availability of the experimental velocity field measurements for use in the CFD validation. Spentzos et al. [24] have performed some numerical simulations for this case and presented some velocity profiles taken from the original experimental data and these profiles are reproduced in the present paper as a validation of the CFD results obtained in this paper, see Fig. 5. In Fig. 5, numerically obtained streamlines are compared with those obtained from the experimental data based on PIV. The number of the streamlines are limited in order to make them easier to be distinguished from each other. For each angle of attack, namely

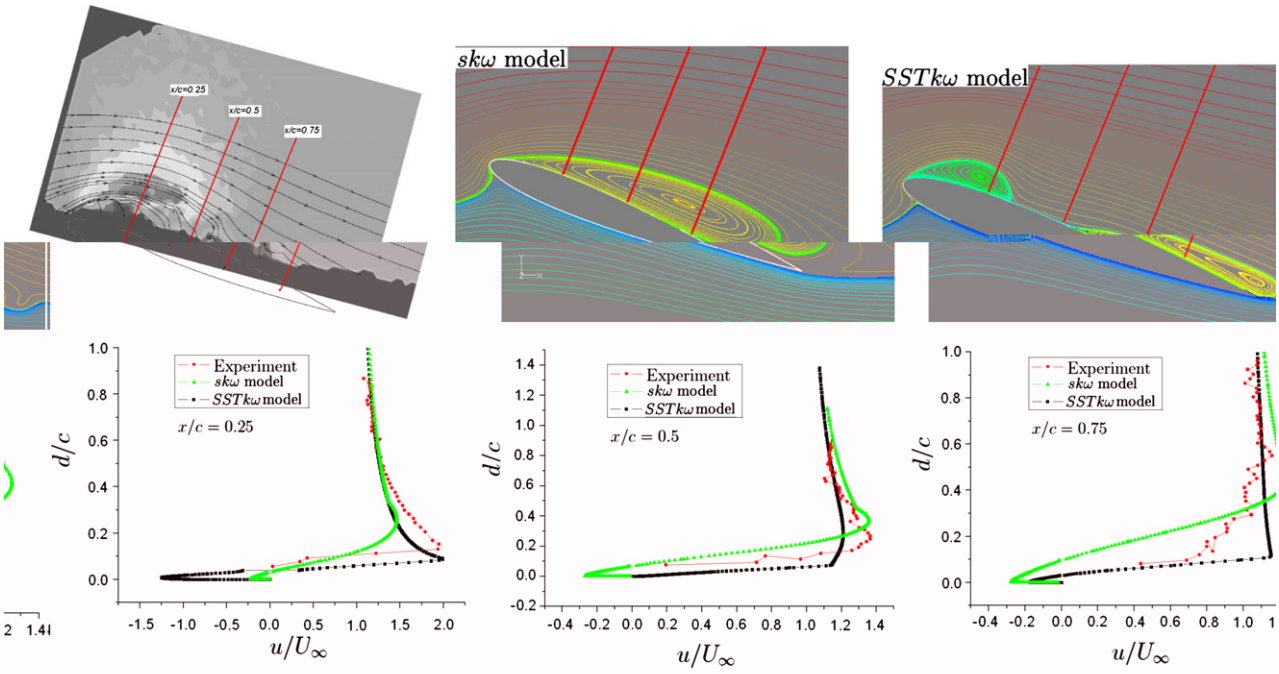

(a) Angle of attack $\alpha = 22^{\circ}$, upstroke.

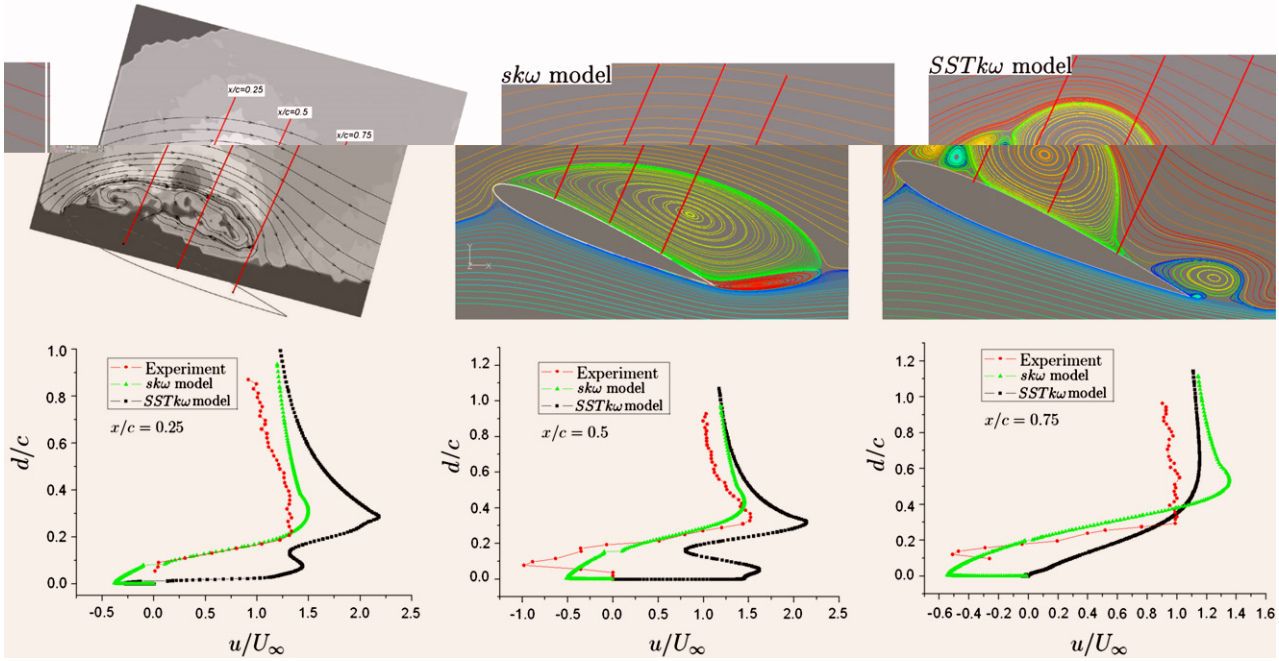

(b) Angle of attack $\alpha = 24^{\circ}$, upstroke.

Fig. 5. Comparison between the numerical results and the experimental data of Wernert et al. [9], Case I.

$\alpha = 22^{\circ}$ and 24°, there are three plots, presenting the variation of the non-dimensional velocity magnitude u/U_{∞} with the non-dimensional distance from the blade d/c, corresponding to three chordwise locations, $x/c = 0.25$, 0.5, 0.75. It should be noted in Fig. 5 that the magnitude of the fluid velocity is assigned a sign, positive meaning the flow goes from the leading edge to the trailing edge and negative meaning the reverse (This assignment is not done for the results of the *SSTkω* model at $\alpha = 24^{\circ}$ since this will cause significant intermittence of the curves).

It can be easily seen from the streamlines that the LEV has been captured by both the *skω* model and the *SSTkω* model, whereas the position and the size of the LEVs obtained by the two models are quite different. In general, the *skω* model generates a more stable flow structure than does the *SSTkω* model and it smears out the small circulations in the near-wall region at $\alpha = 24^{\circ}$. In contrast to the *skω* model, the *SSTkω* model presents a more complex flow structure, especially at a high angle of attack where the two secondary counter-rotating vortices are obtained which appears to be more realistic, since it is also mentioned that small-scale vortices can be recognised on the PIV pictures, even with the large dynamic stall vortex by Wernert et al. [9]. This conclusion has also been obtained by other researchers [8,23,34]. The computed

chordwise spatial extension of about 75% c using the $SSTk\omega$ model is in good agreement with the experimental data. It can be seen that the chordwise dimensions of the vortices in the $SSTk\omega$ model results are much more constrained than those obtained in the $sk\omega$ model, whilst their thickness is much bigger. This may be because the $sk\omega$ model is more dissipative in terms of the eddy energy and fails to predict the severe adverse pressure gradient, making the predicted LEV span a larger portion of the blade. Also a similar conclusion has been drawn by Martinat et al. [31]. Another reason for this may lie in the assumption of fully turbulent flow on the airfoil in the theory of the $sk\omega$ model, whereas the transition in the boundary layer from laminar-to-turbulence at the leading edge of the blade is predicted in the $SSTk\omega$ model. The use of full turbulence models can limit the occurrence of the laminar separation at the leading edge of the airfoil, leading to an inaccurate turbulent flow development, as well as the prediction of the development of the LEV. A comparison of the streamlines obtained from the PIV data shows that the $SSTk\omega$ model clearly performs better than the $sk\omega$ model, which over-predicts the chordwise span of the LEV.

Regarding the comparison between the velocity profiles at the aforementioned three chordwise locations, the results agree better at low angles of attack than at high angles of attack for both models. At high angles of attack the airfoil turns into deep stall and the flow becomes fully separated. For separation flows, the 3D effects should be more significant than those without separations at smaller angles of attack, see [34]. This is where both models fail to match the experimental data. At $\alpha = 22°$, the velocity profile obtained employing the $SSTk\omega$ model at $x = 0.25c$ agrees remarkably well with the experimental data while the $sk\omega$ model fails to capture the maximum velocity and the sharp structure, see Fig. 5a. Compared with the streamlines at this postion, this indicates that the scale and position of the LEV are predicted reasonably well by the $SSTk\omega$ model at lower values of α. At the position of $0.5c$, it can be seen that the $sk\omega$ model still predicts a recirculation in the boundary layer while the LEV has already ended by this point from the results gleaned from the $SSTk\omega$ model. At $x = 0.75c$, the results obtained from the $SSTk\omega$ model agree well with the experimental data in regions further away from the blade and close to the boundary layer. However, the transition of the velocity profile between these two regions appears to be not accurate enough in contrast to the experimental curve. The LEV predicted by the $sk\omega$ model extends even to this chordwise location and clearly this should be an overshoot in the span of the LEV in comparison with the validation data. At high angles of attack, say $\alpha = 24°$, although the $sk\omega$ model appears to present a better trend in comparison with the experimental data, the flow structure differs significantly from the experimental results according to the streamline patterns. Thus, the better agreement with the validation velocity profiles for the $sk\omega$ model may be considered as fortuitous. Further, it should be noted that both of the two numerical models overestimate the magnitude of the velocities in the region further away from the wall where $d/c \geqslant 0.4$.

It should be noted that despite many efforts to eliminate the 3D effects on the testing surface in the experiment, there are still some 3D effects according to the experimental work of Raffel et al. [11], which is based on the same experiment of Wernert et al. [9] if not exactly the same. In addition, because of the limitations in the laser pulse rate and framing speed of the photo camera used in this experiment, it was impossible to record the flow field at all the different angles of attack of the blade within one pitching cycle but in successive periods. What is more, the experimental research was performed twelve years ago, and because of the strong unsteady characteristics of the flow field, the accuracy of the data is still an open question. Potentially, these may be reasons for the discrepancies between the numerical and experimental data.

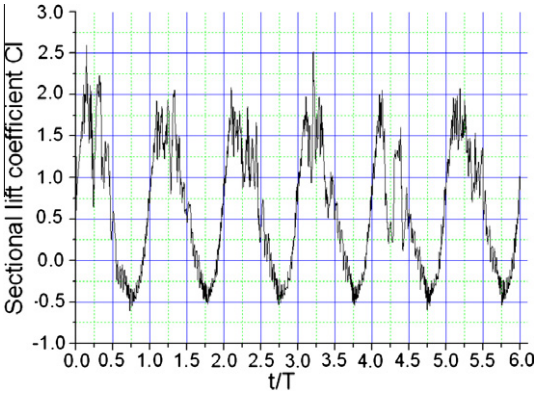

Fig. 6. History of the sectional lift coefficient within six pitching cycles for Case II.

3.2. Simulations of the Lee and Gerontakos [16] test case, Case II

In general, for Case I, the $SSTk\omega$ model produces more accurate predictions than does the $sk\omega$ model and hence this turbulence model is employed in Case II.

Under the operating conditions in this case, a large cycle-to-cycle difference of the solutions at high angles of attack during both the upstroke and downstroke pitching phases is observed. Fig. 6 shows the history of the sectional lift coefficient, C_l, in six pitching cycles starting from the mean angle of attack, i.e. $\alpha = 10°$. This kind of aperiodic or quasi-periodic flow phenomenon is also observed in the experiments [9–11].

The numerically computed coefficients of the aerodynamic forces obtained from a pitching cycle are presented in Fig. 7 and compared with the experimental data. It can be seen that within the range of low and medium angles of attack, i.e. $-5° \leqslant \alpha \leqslant 20°$, the CFD results for the coefficients of aerodynamic forces agree well with the experimental data, fluctuating around the measured data. This is an indication that the $SSTk\omega$ model performs well at these values of angle of attack. However, similar to the results obtained for the case of Wernert et al. [9], Case I, at the high angles of attack, $20° \leqslant \alpha \leqslant 25°$, where deep stall may be expected, the numerical results have a much larger difference from the experimental data.

From Fig. 7a, it is seen clearly that the position of the intersection point 1 between the upstroke and downstroke paths of the sectional lift coefficient at $\alpha \approx 0°$ is well captured by point 1′ as well as the intersection 1 of the sectional drag coefficient in Fig. 7b. However, the absolute values are not exactly the same. Further, the capture of the other intersection, point 2 in Fig. 7b, is not as accurately predicted, and the numerical curve shows a strong instability at high angles of attack.

The reduction in the lift coefficient for $20° < \alpha < 25°$ corresponds to the shedding of the LEV, while there is a sudden increase in the lift coefficient near the maximum angle of attack during the downstroke phase and this is an indication of the generation of the secondary vortex. Firstly, it appears that there is a phase shift between the numerical and experimental results since the secondary vortex appears to occur at about $\alpha = 22°$ in the downstroke motion. This is discussed by McCroskey et al. [12], namely both the strength and phase of the dynamic forces depend upon the reduced frequency k. As shown in Fig. 9, which is adapted from that presented by McCroskey et al. [12], as k increases, the phase of the normal force curve shifts to the right, or rather it causes a delay in the phase of the dynamic stall. At $k = 0.05$, both the shedding of the LEV and the generation of the secondary vortex occurs before the maximum angle of attack when the blade is still in the upstroke phase. At $k = 0.15$, the occurrence of the secondary vortex has already been

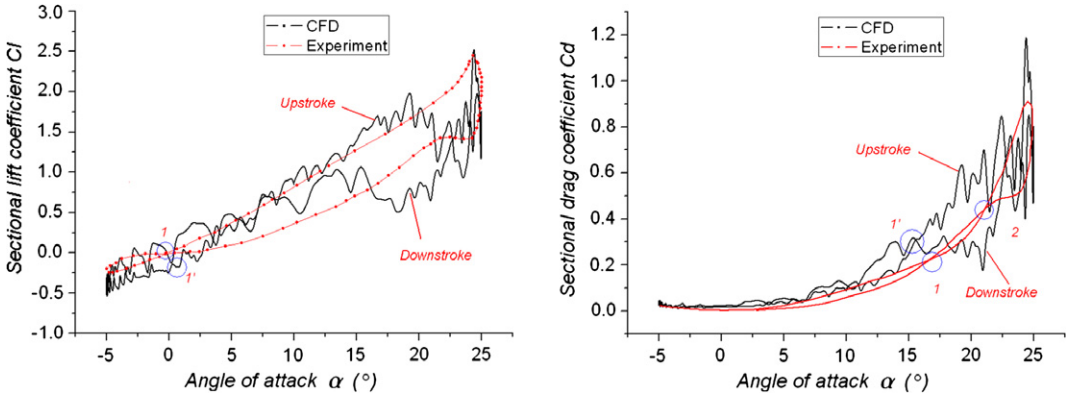

(a) The sectional lift coefficient (b) The sectional drag coefficient

Fig. 7. Comparison of the sectional lift and drag coefficients hysteresis loops between the CFD and experiments by Lee and Gerontakos [16], Case II.

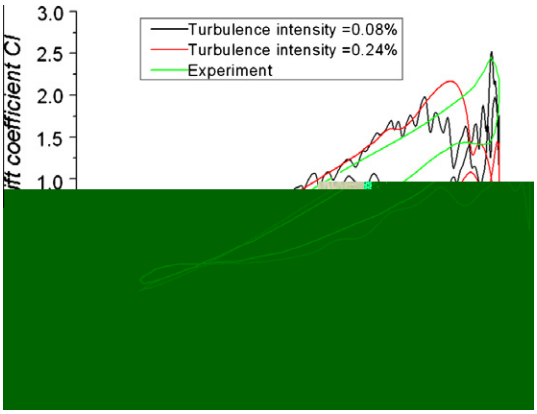

Fig. 8. Comparison of the computed sectional lift coefficients for the two turbulence intensity levels, Case II.

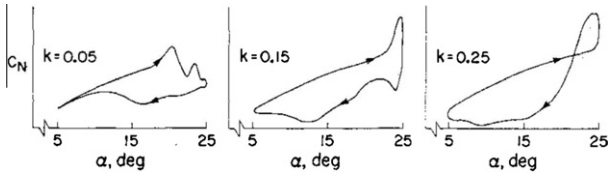

Fig. 9. Comparison of the normal forces between different reduced frequencies [12].

postponed into the downstroke section and, at $k = 0.25$, even the shedding of the LEV occurs in the downstroke phase. It appears that the maximum value of the lift also increases with an increase of k within the range $0.05 < k < 0.15$. Based on this conclusion, it appears that the numerical results for $k = 0.10$ correspond to those with a lower value of k.

It is found that free stream turbulence intensity has a significant impact on the stability/fluctuations of the numerically predicted lift coefficient curves at the small frequencies investigated in Case II, as shown in Fig. 7. Therefore, a test is performed by changing the turbulence intensity of the free stream from the original value 0.08–0.24% and the results obtained are depicted in Fig. 8. It is observed that the sectional lift coefficient curve becomes smooth on increasing the turbulence intensity. Again, this indicates that the numerical simulations are in very good agreement with the experimental data at low angles of attack. The results suggest that a higher free stream turbulence level would improve the stability of the predicted forces on the blade at small AoA ($-5° \leqslant \alpha \leqslant 5°$) and also assist in the delay of stall at larger AoA ($\alpha > 20°$). This may be a contribution made by the improved energy transfer across the boundary layers that delays the laminar-to-turbulent boundary layer transition as well as the flow separation. In addition, the oscillations in the lift coefficients at small AoA, where the flow is assumed to be non-separated, imply that the *SSTkω* model is very sensitive in the present unsteady low turbulence intensity flow application.

3.3. Flow development under deep dynamic stall conditions

In this section, in order to assist in the further understanding the complex behaviour of the flow during the dynamic stall process, details of the numerically simulated development of the flow structure under deep dynamic stall conditions at low Reynolds number are presented for Cases I and II.

3.3.1. Flow development for Case I

3.3.1.1. Dynamic stall process. Fig. 10 demonstrate the non-dimensional vorticity fields (Ω') for different angles of attack through a full pitching cycle in Case I. The corresponding streamlines are shown in Fig. 11 for a better interpretation of the results. It is observed that the flow structures at different stages of the developments of the LEV is qualitatively in good agreement with the observations of other researchers [23,31]. From the angles of attack $\alpha = 5$–$17.6°$, the flow remains fully attached to the airfoil, other than for a small laminar separation bubble that occurs near the leading edge. The spatial extension of the bubble can be detected by exploring the skin friction coefficient near the leading edge of the airfoil, which is not presented here. One feature of the dynamic stall, which is the delay of lift stall to angles beyond the static angle of attack ($\alpha \approx 16°$ [11]) appears clearly here. Then from about $\alpha = 20°$, a reversed flow occurs at the trailing edge and this can be observed from Fig. 11, and also from Fig. 10d, where the vorticity layer on the suction surface of the airfoil is detached from the trailing edge. The adverse pressure gradient that causes the flow reversal appears to be mainly due to the rapid movement of solid boundary, say the trailing edge, especially at such a low Reynolds number studied in this case. At an angle of attack $\alpha = 22°$, the LEV has already formed at the leading edge and the strength of the recirculation has increased. Then the LEV breaks into two small counter-rotating vortices, which indicate that the boundary layer at the leading edge is quite unstable, see Fig. 10f and Fig. 11. The complex structure within the LEV is also reported by Raffel et al. [34]. The trailing edge vortex formed previously now becomes

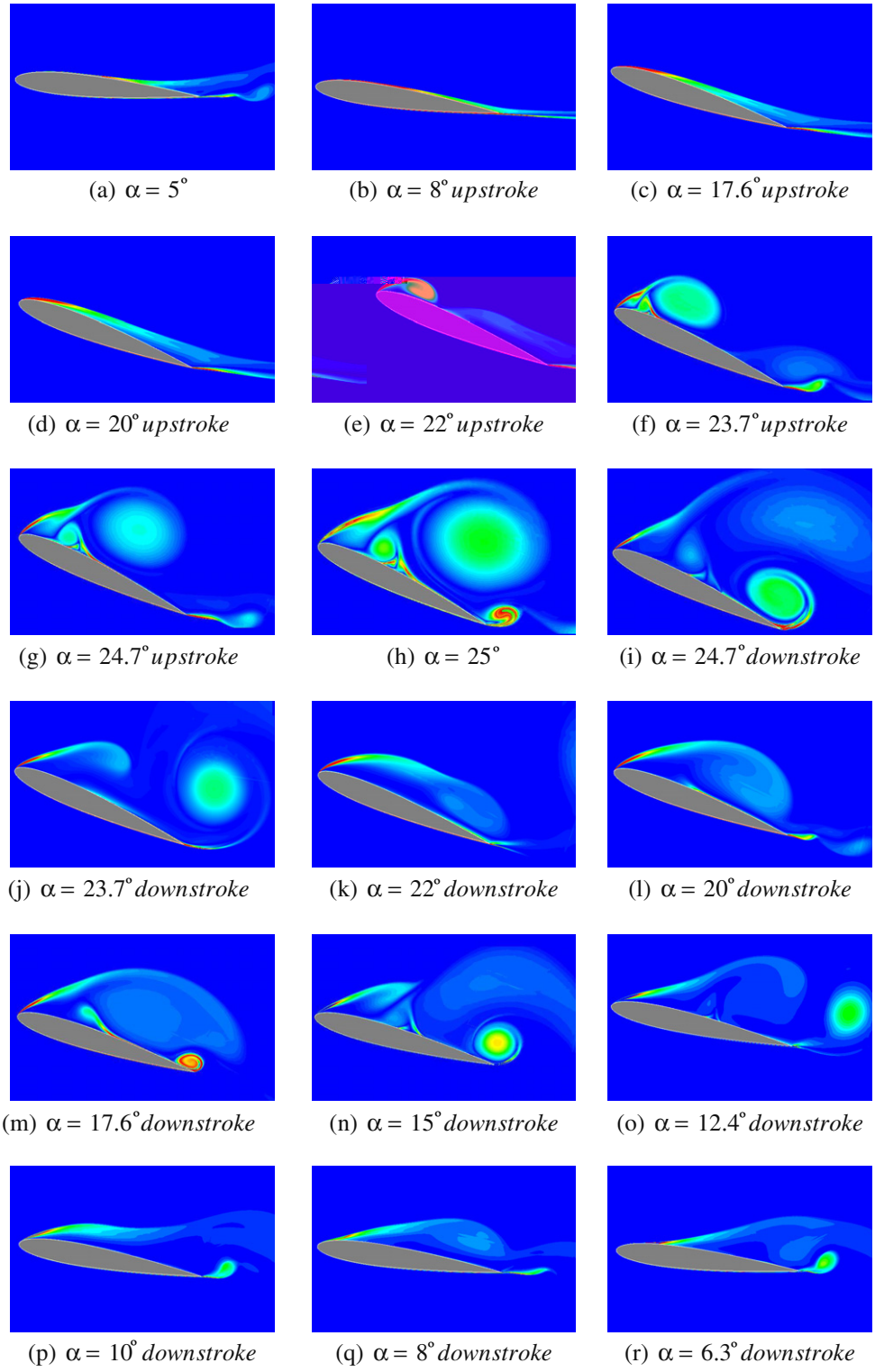

Fig. 10. Non-dimensional vorticity field for the upstroke pitching phase using the *SSTkω* model in Case I.

more compact and starts to slowly travel downstream. Meanwhile, another small circulation occurs next to the trailing edge vortex. However, this circulation is formed by the suction side flow, rather than the rolling up vortex of the trailing edge, see Fig. 11. At an angle of attack $\alpha = 24.7°$, the two vortices that were previously at the trailing edge have now been shed into the wake and the rolling-up vortex that penetrated from the pressure side of the airfoil into the suction side flow has been initiated. At this time, the LEV has covered the whole span of the suction side of the blade and the highest value of the lift coefficient is obtained, see Fig. 12. When the airfoil approaches its maximum angle of attack, $\alpha = 25°$, the LEV continues convecting and is seen to separate from the suction surface while the other three vortices keep growing in size. It is clearly seen from Fig. 12 that the shedding of the LEV causes a sudden lift stall. It should be noted that the magnitude of the vorticity of the rolling-up vortex becomes significant and the flow from the

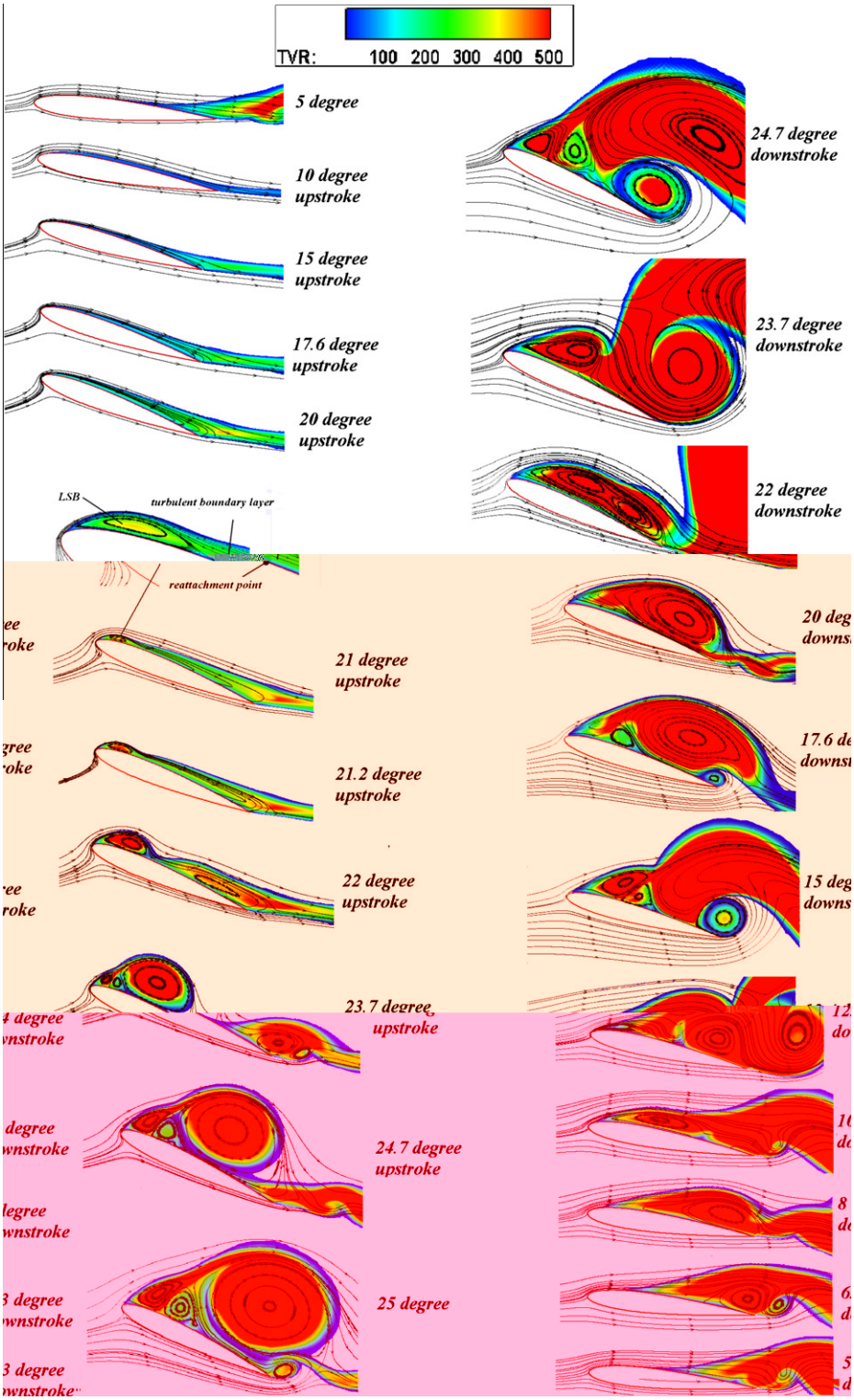

Fig. 11. Turbulent viscosity field with flow streamlines for a pitching cycle for Case I.

pressure side of the airfoil is rolled up into the suction side and mixes with the shedding LEV. Then the blade begins to retreat. At $\alpha = 24.7°$, the rolling-up counter-clockwise vortex that penetrated from the trailing edge, grows much bigger and interacts in a complex manner with the clockwise LEV which is detached from the blade. Then, the rolling-up vortex is shed into the wake. The two counter-rotating vortices at the leading edge join together into one vortex at $\alpha = 23.7°$ and it dominates the suction surface until $\alpha = 20°$. According to the experiments of Raffel et al. [11] and Leishman [10], this should be the secondary vortex which leads to a significant increase in the lift during the downstroke motion and is a characteristic feature of the dynamic stall process at low free stream Mach numbers. The lift increase is clearly seen in the sectional lift coefficient curve in Fig. 12. The lift during the downstroke phase reaches its maximum value at $\alpha = 20°$ when the strength of the secondary vortex maximises. At the angle of attack

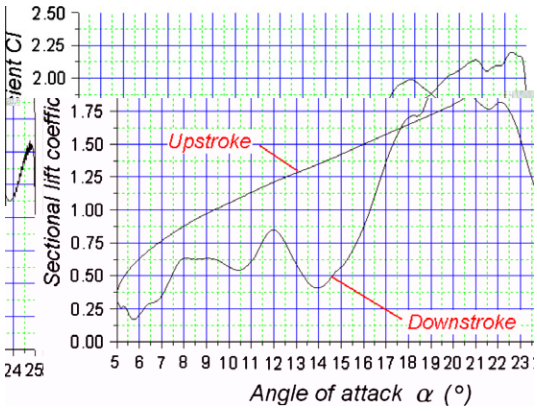

Fig. 12. The computed sectional lift coefficient of Case I.

$\alpha = 17.6°$, the vortex begins to detach from the blade surface while another pair of couner-rotating vortices appear at the leading edge and a second rolling-up vortex forms at the trailing edge. Eventually, all these vortices convect to the wake. The last vortex leaves the suction surface at $\alpha = 6.3°$, and the flow completely reattaches to the airfoil only when the blade returns to its minimum angle of attack, $\alpha = 5°$. Therefore, there is a considerable delay in the flow attachment during the downstroke.

3.3.1.2. Transition development. For low Reynolds number flows, as studied in this paper, laminar-to-turbulent boundary-layer transition may play a significant role in the unsteady flow characteristics [34–36]. Under low Reynolds number conditions, the boundary layer at the leading edge of the airfoil may still be laminar, and thus it is unable to resist severe adverse pressure gradients and hence the flow is subject to separation from the airfoil. The separated, but still laminar, flow is highly sensitive to disturbances and hence experiences laminar-to-turbulent transition. Due to the ability of the turbulent boundary layer to negotiate the pressure gradient, the flow may reattach to the airfoil and form the so-called laminar separation bubble (LSB). This bubble may grow in size and strength with an increase in the incidence angle and eventually this causes the leading-edge type of dynamic stall [12].

Because, in the $k-\omega$ turbulence models, the Reynolds stresses are not modelled and therefore only the turbulent viscosity μ_t is available to analyse the flow turbulence characteristics. Usually, the turbulent viscosity is at least two orders of magnitude larger than the molecular viscosity for fully developed turbulent flows modelled using the RANS approach [33]. Based on this point of view, and by observing the numerical field for the turbulent viscosity ratio,TVR, defined by μ_t/μ, as shown in Fig. 11, it is reasonable to assume that in the present case the transition region corresponds to the TVR value between 200 and 300. The field for the TVR is inspected in order to qualitatively identify the transition development near the suction surface of the airfoil. Fig. 11 clearly shows that in the upstroke phase, when the angles of attack are moderately high ($\alpha < 18°$), the flow is laminar on the suction surface of the airfoil. When α reaches about 20°, the transition appears to occur at the trailing edge. At $\alpha = 21°$, in addition to the upstream movement of the trailing edge transition region, a laminar separation bubble (LSB) is formed and the transition within the LSB can be clearly observed.

The turbulence intensity grows as the growth of the LSB or rather the LEV with an increase in α. However, it should be observed that there appears to be a relaminarization zone shortly after the LSV, as shown in the situation when $\alpha = 22°$ and 23.7°. It can be seen that the vortices are the main sources of turbulence when $\alpha = 23–25°$. However, it is interesting to note that the turbulence intensity of the vortex behind the left-most vortex is not strong as it is protected by the upstream vortex. It should be noted that the turbulence intensity of the flow near the pressure surface of the airfoil is very low and this explains why the rolling-up vortex from the pressure surface produces a low turbulence region near the trailing region of the suction surface, as shown at $\alpha = 25°$, 24.7°*downstroke*, 17.6°*downstroke* and 15° *downstroke*. Unlike in the upstroke phase, the downstroke phase is more turbulent since the fully turbulent region still covers more than one half of the airfoil chord, even at $\alpha = 8°$ at which the flow is almost laminar in the upstroke phase. The transition point retreats from the leading edge $x \approx 0.2c$ to the trailing edge $x \approx 0.75c$, as shown from $\alpha = 8–5.3°$.

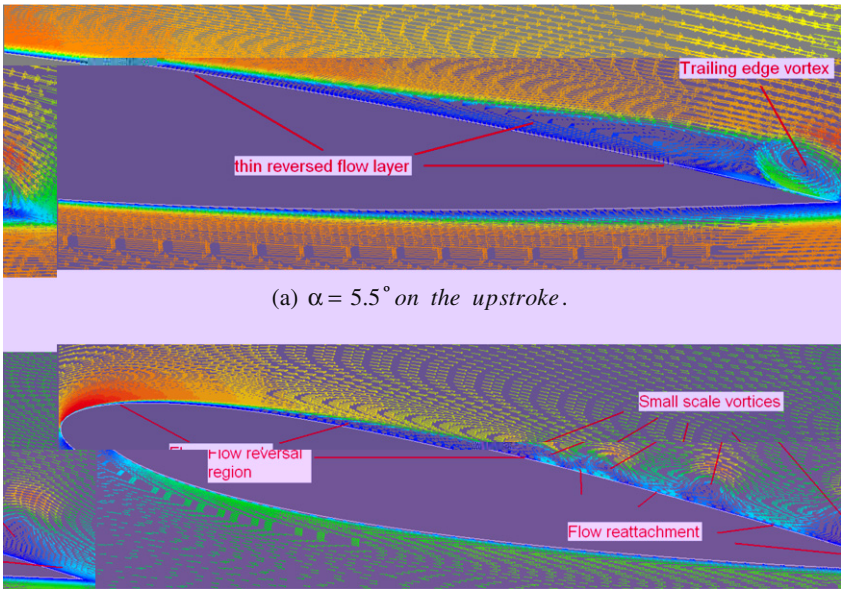

Fig. 13. Velocity vectors around the airfoil for Case II. (a) $\alpha = 5.5°$ on the upstroke, (b) $\alpha = 10°$ on the upstroke.

3.3.2. Flow development for Case II

One feature of the flow development of Case II is the rear-to-front progression of the trailing edge flow reversal before the occurrence of the dynamic stall, which is observed in the experiment [16]. Further McCroskey et al. [12] also reported investigations of the dynamic stall associated with this kind of flow behaviour. Fig. 13a shows the computed thin flow reversal layer near the trailing edge on the suction side, which extends to about $0.5c$ from the trailing edge at $\alpha = 5.5°$. This reversal gradually propagates towards the leading edge as the AoA increases and reaches about $0.1c$ from the leading edge at $\alpha = 10°$ on the upstroke, as shown in Fig. 13. It should be noted that the thin layer of reversed flow near the suction side is significantly unstable and easily breaks down into several small-scale vortices which can be seen in Fig. 13. As in the LEV, these small vortices also carry pressure waves, despite the strength being much smaller than the LEV. This appears to be responsible for the oscillations of the aerodynamic loads shown in Fig. 7.

Another characteristic of the stall process observed in Case II is that the stall is trigged by a turbulent separation at a short distance downstream of the leading edge bubble, rather than by the burst of the bubble. This feature is also well captured by the simulations, since it can be clearly seen from the computed flow field that the leading edge bubble maintains its existence to a very high angle of attack. However it appears from the numerical data that the leading edge bubble is induced to shed vortices from time to time. The effect of the continuous shedding is similar to the turbulent breakdown as discussed by Lee and Gerontakos [16]. However, the predicted onset of the lift stall is earlier than that observed in the experiments which indicates that the shedding of the LEV is not accurately simulated.

In this section, the flow development events have been discussed and the computational results qualitatively capture well the features of the dynamic stall process, such as the formation, convection and shedding of the LEV as well as the secondary vortex, and these predictions can provide detailed information on the flow development.

4. Conclusions

In this study, two URANS models, namely the *standard* $k-\omega$ model and the *SST* $k-\omega$ model with transition, have been employed to simulate the fluid flow around two sinusoidally pitching NACA0012 airfoils, in the context of the low Reynolds number regime, $Re \approx 10^5$. The *standard* $k-\omega$ model appears too dissipative to predict the severe adverse pressure gradient near the suction side of the blade and this causes an over-prediction of the LEV span in the chordwise direction and an underestimate of the thickness of the LEV. The *SST* $k-\omega$ model presents an improvement over the *standard* $k-\omega$ model and can predict the experimental data with reasonable accuracy, other than at very high angles of attack where the flow is fully detached and the 3D effect is expected to be more significant. The characteristics of dynamic stall, such as the LEV-dominated flow structure, the aerodynamic load hysteresis loops, and the secondary vortex in the downstroke phase, is well captured by the *SST* $k-\omega$ model. In addition, a fairly reasonable development of the flow transition before and during the dynamic stall can be numerically obtained. In order to obtain a very detailed understanding of the details of the dynamic stall phenomenon, the capability of other more advanced CFD methods, such as LES or DES, needs to be investigated. In particular for the investigation of the blade/wake interactions in the core of VAWTs, detailed and accurate simulations of the vortex formation and shedding in both low and high AoA in a transient state needs to be investigated. However, URANS with advanced turbulence models, such as the *SST* $k-\omega$ model as evaluated in this paper, are useful for the fast design or research intension for low Reynolds number airfoils and VAWTs, because they are capable of capturing the experimental data in a significant part of the flow dynamics.

Acknowledgements

The authors would like to acknowledge the financial support from the Chinese Scholarship Council (CSC) for this work. Also the authors would like to thank Dr. G. Barakos from The University of Liverpool, UK, Professor T. Lee from McGill University, Canada, Mr. Wolfgang Geissler from German Aerospace Centre (DLR) and Dr. Philippe Wernert from the French–German Research Institute of Saint-Louis (ISL), Germany, for their kind support of the research associated with this paper.

References

[1] Blackwell B. Vertical-axis wind turbine: how it works. Technical report, SLA-74-0160, Sandia Labs., Albuquerque, N. Mexico (USA); 1974.
[2] Paraschivoiu I. Wind turbine design: with emphasis on Darrieus concept. Canada: Polytechnic International Press; 2002.
[3] Ferreira C, Bijl H, van Bussel G, van Kuik G. Simulating dynamic stall in a 2D VAWT: modeling strategy, verification and validation with particle image velocimetry data. J Phys Conf Ser 2007;75.
[4] Edwards J, Durrani N, Howell R, Qin N. Wind tunnel and numerical study of a small vertical axis wind turbine. In: 46th AIAA aerospaces sciences meeting and exhibit, Reno, Nevada, vol. 11; 2008.
[5] Simão Ferreira C, van Kuik G, van Bussel G, Scarano F. Visualization by PIV of dynamic stall on a vertical axis wind turbine. Exp Fluids 2008;46(1):97–108.
[6] Carr L. Progress in analysis and prediction of dynamic stall. J Aircraft 1988;25(1):6–17.
[7] Allet A, Halle S, Paraschivoiu I. Numerical simulation of dynamic stall around an airfoil in Darrieus motion. J Sol Energy 1999;121:69–76.
[8] Cebeci T, Platzer M, Chen H, Chang K-C, Shao JP. Analysis of low speed unsteady airfoil flows. Long Beach, California, US and Heidelberg, Germany: Horizons Publishing; 2005.
[9] Wernert P, Geissler W, Raffel M, Kompenhans J. Experimental and numerical investigations of dynamic stall on a pitching airfoil. AIAA J 1996;34(5):982–9.
[10] Leishman J. Dynamic stall experiments on the NACA 23012 aerofoil. Exp Fluids 1990;9(1):49–58.
[11] Raffel M, Kompenhans J, Wernert P. Investigation of the unsteady flow velocity field above an airfoil pitching under deep dynamic stall conditions. Exp Fluids 1995;19(2):103–11.
[12] McCroskey W, Carr L, McAlister K. Dynamic stall experiments on oscillating airfoils. AIAA J 1976;14(1):57–63.
[13] McCroskey W, McAlister K, Carr L, Pucci S. An experimental study of dynamic stall on advanced airfoil sections. Summary of the experiment, vol. 1. NASA Technical Memorandum 84245; 1982.
[14] McAlister K, Pucci S, McCroskey W, Carr L. An experimental study of dynamic stall on advanced airfoil section. Pressure and force data, vol. 2. NASA Technical Memorandum 84245; 1982.
[15] Schreck S, Helin H. Unsteady vortex dynamics and surface pressure topologies on a finite pitching wing. J Aircraft 1994;31(4):899–907.
[16] Lee T, Gerontakos P. Investigation of flow over an oscillating airfoil. J Fluid Mech 2004;512:313–41.
[17] Wu J, Sankar L, Huff D. Evaluation of three turbulence models for the prediction of steady and unsteady airloads. In: AIAA, the 27th aerospace sciences meeting, Reno, NV; 1989.
[18] Visbal M. Dynamic stall of a constant-rate pitching airfoil. J Aircraft 1990;27(5):400–7.
[19] Tuncer I, Wu J, Wang C. Theoretical and numerical studies of oscillating airfoils. AIAA J 1990;28(9):1615–24.
[20] Ekaterinaris J. Numerical investigation of dynamic stall of an oscillating wing. AIAA J 1995;33(10):1803–8.
[21] Srinivasan G, Ekaterinaris J, McCroskey W, Aeronautics N, Administration S, States U. Evaluation of turbulence models for unsteady flows of an oscillating airfoil. Comput Fluids 1995;24(7):833–61.
[22] Mellen C, Frohlich J, Rodi W. Lessons from LESFOIL project on large-eddy simulation of flow around an airfoil. AIAA J 2003;41(4):573–81.
[23] Barakos G, Drikakis D. Computational study of unsteady turbulent flows around oscillating and ramping aerofoils. Int J Numer Methods Fluids 2003;42(2):163–86.
[24] Spentzos A, Barakos G, Badcock K, Richards B, Wernert P, Schreck S, et al. Investigation of three-dimensional dynamic stall using computational fluid dynamics. AIAA J 2005;43(5):1023–33.
[25] Sheng W, Galbraith R, Coton F. A modified dynamic stall model for low mach numbers. J Sol Energy – Trans ASME 2008;130(3):031013.
[26] McCroskey W. The phenomenon of dynamic stall. NASA TM-81264; 1981.
[27] McCroskey W. Unsteady airfoils. Annu Rev Fluid Mech 1982;14(1):285–311.

[28] Niu Y. Evaluation of renormalization group turbulence models for dynamic stall simulation. AIAA J 1999;37(6):770–1.
[29] Wilcox D. Turbulence modeling for CFD. DCW Industries, La Canada, CA.
[30] Menter F. Two-equation eddy-viscosity turbulence models for engineering applications. AIAA J 1994;32(8):1598–605.
[31] Martinat G, Braza M, Hoarau Y, Harran G. Turbulence modelling of the flow past a pitching NACA0012 airfoil at 10^5 and 10^6 Reynolds numbers. J Fluid Struct 2008;24(8):1294–303.
[32] Fluent I. Fluent 6. 3 user's guide. Fluent documentation.
[33] Ansys F. Fluent user's manual. Software release 6.
[34] Raffel M, Favier D, Berton E, Rondot C, Nsimba M, Geissler W. Micro-PIV and ELDV wind tunnel investigations above a helicopter blade tip. Measur Sci Technol 2006;17:1652–8.
[35] Geissler W, Chandrasekhara M, Platzer M, Carr L. The effect of transition modelling on the prediction of compressible deep dynamic stall. In: 7th Asian congress of fluid mechanics; 1997.
[36] Lissaman P. Low-Reynolds-number airfoils. Annu Rev Fluid Mech 1983;15(1):223–39.